journal of the mechanical behavior of biomedical materials 150 (2024) 106271

Contents lists available at ScienceDirect

Journal of the Mechanical Behavior of Biomedical Materials

journal homepage: www.elsevier.com/locate/jmbbm

# Accuracy meets simplicity: A constitutive model for heterogenous brain tissue

Nicholas Filla [a], Jixin Hou [a], Tianming Liu [b], Silvia Budday [c], Xianqiao Wang [a,*]

[a] School of ECAM, College of Engineering, University of Georgia, Athens, GA, 30602, USA
[b] School of Computing, University of Georgia, Athens, GA, 30602, USA
[c] Institute of Applied Mechanics, Department of Mechanical Engineering, Friedrich-Alexander-Universität Erlangen-Nürnberg, Erlangen, Germany

A B S T R A C T

We present a general, hyperelastic, stretch-based potential that shows promise for modeling the mechanics of brain tissue. A specific four-parameter model derived from this general potential outperforms alternative models, such as the modified Ogden model, the Gent model, Demiray model, and machine-learning models, in capturing brain tissue elasticity. Specifically, the stretch-based model achieved $R^2$ values of 0.997, 0.992, and 0.993 (tension, compression, and shear) for the cortex, 0.995, 0.983, and 0.983 for the basal ganglia, 0.994, 0.929, and 0.970 for the corona radiata, and 0.990, 0.896, and 0.969 for the corpus callosum. This work has the potential to advance our understanding of brain tissue mechanics and provides a valuable tool to improve finite element models for the investigation of brain development, injuries, and disease.

## 1. Introduction

In recent years, the study of the interplay between brain mechanics and brain diseases, injuries, and development has gained significant prominence within the scientific community. The World Health Organization considers neurological disorders a matter of utmost concern for public health. Every year, millions of people are subject to traumatic brain injury (MacManus et al., 2018), with ~50,000 fatalities recorded in the United States (Faul et al., 2010) and ~56,000 fatalities recorded in Europe (Majdan et al., 2016) per annum. Additionally, alterations in the mechanics of the brain have been shown to result in cortical malformations (Budday et al., 2014, 2015) linked to various disorders including schizophrenia (Harrison, 1999), autism (Nordahl et al., 2007), and epilepsy (Blümcke et al., 2009), as well as to cell death in patients with Alzheimer's disease correlated to progression of dementia (Blumenthal et al., 2014) (See the review (Budday et al., 2020)).

Furthermore, mechanics have been demonstrated to play a vital role in both neuronal function and dysfunction (Goriely et al., 2015; Barnes et al., 2017), as stresses may regulate the developmental processes (Barnes et al., 2017; Tallinen et al., 2016; Razavi et al., 2015) and the progression of neurological disease (Barnes et al., 2017; Jalil Razavi et al., 2015). Thus, it is imperative to accurately characterize the mechanical properties of brain tissue in the field of biomechanics.

The study of brain tissue mechanics is a vital pursuit in comprehending the intricacies of the mechanobiological processes of the brain. The use of computational models and personalized simulations grants a deeper understanding and lessens the reliance upon animal and human experiments. Yet, a precise understanding of these processes demands models of great accuracy, capable of encapsulating the complexity of brain tissue's elastic and viscoelastic properties.

The time-independent behavior of brain tissue is the primary concern of this paper. Many strain-energy functions have been investigated for their ability to describe brain tissue elasticity, such as the neo-Hookean (Budday et al., 2020; Linka et al., 2022; Mihai et al., 2015; Pierre et al., 2023), Mooney-Rivlin (Mihai et al., 2015; Pierre et al., 2023), Ogden (Budday et al., 2020; Mihai et al., 2015; Pierre et al., 2023; Rashid et al., 2014), Fung (Mihai et al., 2015; Rashid et al., 2014), Blatz-Ko (Linka et al., 2022; Pierre et al., 2023), Holzapfel (Linka et al., 2022), Gent (Budday et al., 2020; Mihai et al., 2015; Rashid et al., 2014), and Demiray (Budday et al., 2020; Linka et al., 2022) models. However, when tasked with describing the behavior of tension, compression, and shear simultaneously, the limitations of these models become apparent (Budday et al., 2020; Linka et al., 2022; Pierre et al., 2023). To this end, recent efforts have turned to machine learning in the pursuit of comprehensive elasticity potentials, offering not only a promising means of identifying material models, but also a promising approach to describing the elasticity of brain tissue (Linka et al., 2022; Pierre et al., 2023; Linka and Kuhl, 2023). Regardless of the approach or form, an increasing accuracy of comprehensive material models for brain tissue is required.

* Corresponding author.
*E-mail address:* xqwang@uga.edu (X. Wang).

https://doi.org/10.1016/j.jmbbm.2023.106271
Received 16 March 2023; Received in revised form 3 October 2023; Accepted 22 November 2023
Available online 25 November 2023

In this work, we present a general, $n$-term, hyperelastic, stretch-based strain energy function. Through close examination, a specific four-parameter constitutive model was isolated, demonstrating great efficacy in modeling the time-independent properties of the brain. This model was found to possess an exceptional ability to describe the tensile, compressive, and shear stresses experimentally recorded for human brain tissue from the cortex, basal ganglia, corona radiata, and corpus callosum. This work may contribute to a better phenomenological treatment of brain tissue elasticity, providing a valuable instrument for improving finite element simulations to study morphological changes, malformations, and injuries of brain tissues. Furthermore, the integration of this potential into automated material model discovery may serve to increase the accuracy of future machine-learned models, further advancing our comprehension of the brain's mechanics.

## 2. Theoretical foundation and developments

### 2.1. Principal-stretch-based strain energy density function

This inquiry was initiated after considering strain energy density as a polynomial expansion of the Biot strain measure,

$$\psi = \sum_{k=2}^{n} \sum_{i=1}^{3} \beta_k (\lambda_i - 1)^k \tag{1}$$

where $\psi$ denotes the strain energy density, $\lambda_i$ denotes the principal stretches, $\beta_k$ represents a scalar coefficient, and $k$ is an integer that exponentiates the Biot strain. The stress due to simple tension or compression may be written as,

$$P_{11} = \sum_{k=1}^{n} k\beta_k \left( (\lambda - 1)^{k-1} - \frac{1}{\lambda^{3/2}} \left( \frac{1}{\sqrt{\lambda}} - 1 \right)^{k-1} \right) \tag{2}$$

where $\lambda$ is the stretch in the tensile direction, while the stress due to simple shear can be written as,

$$P_{12} = \sum_{k=1}^{n} k\beta_k \left( \frac{\lambda^2}{\lambda^2 + 1} (\lambda - 1)^{k-1} - \frac{\lambda^{-2}}{\lambda^{-2} + 1} \left( \frac{1}{\lambda} - 1 \right)^{k-1} \right) \tag{3}$$

where $\lambda = \sqrt{\frac{1}{2}(2 + \gamma^2 + \gamma\sqrt{4 + \gamma^2})}$ and $\gamma$ is the amount of shear. The derivations of engineering stresses, $P_{11}$ and $P_{12}$, are presented in Appendices A and B. These appendices provide an examination of the fundamental continuum mechanics required to derive Equations (2) and (3), starting from Equation (1). Appendix A encompasses an examination of the kinematic definitions necessary for this study, while Appendix B delves into the intricacies of deriving stress in simple tension/compression and shear from a hyperelastic potential.

Lastly, to be consistent with linear elasticity the term resulting from $k = 1$ is skipped and the shear modulus is equal to $\beta_2$. For this reason, the term resulting from $k = 2$ must be present in the strain energy function and $\beta_2$ must be strictly greater than zero. The equations used for identifying the consistency conditions of this model are presented in Appendix C.

### 2.2. Polyconvexity

It is important to consider the convexity of strain energy functions for the set of all admissible deformations i.e. $\lambda_1 > 0$, $\lambda_2 > 0$, and $\lambda_3 > 0$. To ensure polyconvexity, the strain Hessian matrix of the strain energy function with respect to its independent variables,

$$H(\lambda_1, \lambda_2, \lambda_3) = \begin{bmatrix} \frac{\partial^2 \psi}{\partial \lambda_1^2} & \frac{\partial^2 \psi}{\partial \lambda_1 \partial \lambda_2} & \frac{\partial^2 \psi}{\partial \lambda_1 \partial \lambda_3} \\ \frac{\partial^2 \psi}{\partial \lambda_2 \partial \lambda_1} & \frac{\partial^2 \psi}{\partial \lambda_2^2} & \frac{\partial^2 \psi}{\partial \lambda_2 \partial \lambda_3} \\ \frac{\partial^2 \psi}{\partial \lambda_3 \partial \lambda_1} & \frac{\partial^2 \psi}{\partial \lambda_3 \partial \lambda_2} & \frac{\partial^2 \psi}{\partial \lambda_3^2} \end{bmatrix} \tag{4}$$

must be a positive definite matrix, i.e., it should be symmetric and all of its eigenvalues are strictly greater than zero. The mixed partial derivatives of Equation (1) are uniquely zero and therefore the Hessian is a symmetric, diagonal matrix $H = diag\left[\frac{\partial^2 \psi}{\partial \lambda_1^2}, \frac{\partial^2 \psi}{\partial \lambda_2^2}, \frac{\partial^2 \psi}{\partial \lambda_3^2}\right]$. Consequently, its eigenvalues, $\frac{\partial^2 \psi}{\partial \lambda_i^2}$, are used to evaluate the polyconvexity of particular strain energy density functions from Equation (1): as long as the eigenvalues are not complex or negative, the strain energy density will be polyconvex.

### 2.3. Brain tissue data and analysis

This study will use the tension, compression, and shear data of human brain tissue from various regions, i.e., the cortex, basal ganglia, corona radiata, and corpus callosum, as reported in the reference (Budday et al., 2017a) and tabulated in reference (Linka et al., 2022). Our models were concurrently fitted against these aforementioned data, yielding $R^2$ values for each of the deformation modes, namely $R_T^2$ for tension, $R_C^2$ for compression, and $R_S^2$ for shear. The parameters for each model regressed here were found by minimizing the relative squared residuals as suggested by Destrade et al. since the relative residuals are non-dimensional and identical for all stress measures while absolute residuals are dependent on the choice of stress measure and may lead to stress-measure-specific parameter sets and accuracy (Destrade et al., 2017). The calculation of the coefficients of determination, $R^2$, was performed through, $1 - \frac{RSS}{TSS}$, with RSS being the residual sum of squared errors and TSS the total sum of squares. In determining the appropriate model, Akaike's information criteria (AIC) was employed to evaluate the models' ability to fit the brain tissue data while avoiding overfitting. The calculation of AIC was performed through $Nln\left(\frac{RSS}{N}\right) + 2n$, where $N$ represents the total number of data points and $n$ represents the number of adjustable parameters in the model.

## 3. Results and discussions

### 3.1. Effect of terms in model selection

To identify the precise model for brain tissue from Equation (1), the method of multiple linear regression was employed. The powers 2 through 10 of the strain energy density function (first nine terms) were taken into consideration, and all possible combinations of these terms were assessed for their proficiency in forecasting the stresses generated in brain tissue from the cortex under tension, compression, and shear. It was noted that the accuracy of the model did not significantly improve upon the inclusion of five terms. The outcomes of the most precise models, ranging from one to five terms, are depicted in Fig. 1 and Table 1.

Through examination, the AIC derived from the regression showed no improvement when terms exceeded four from the subset of terms with powers ranging from 2 to 10 (see Table 1). The likelihood that the

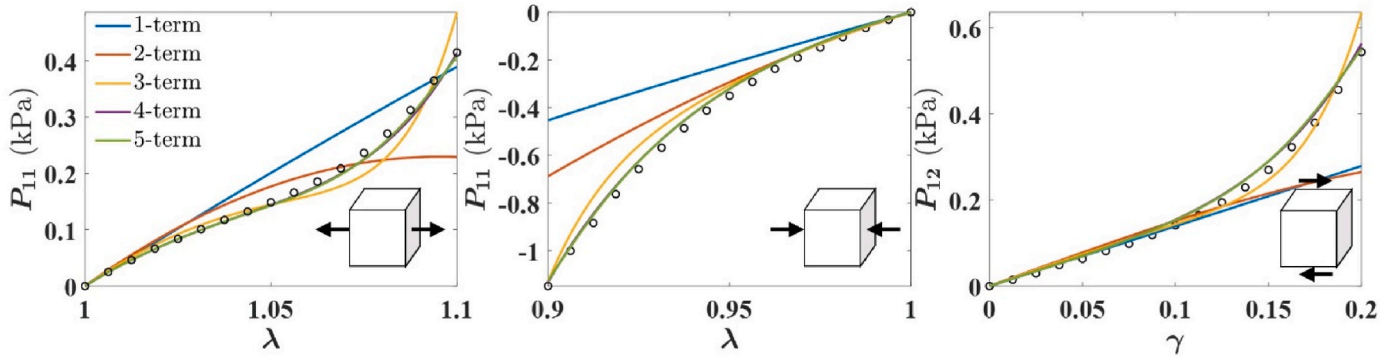


**Fig. 1.** The best 1, 2, 3, 4, and 5 term strain energy density functions (solid lines) identified from multiple linear regression against tension, compression, and shear data from the cortex (black circles). Three terms were required to reach appreciable accuracy. Four terms achieve great accuracy, and the fifth term only slightly improves the model.

four-term model minimizes information loss was inconclusive when compared to the five-term model, as indicated by the relative likelihood of the five-term model, $e^{\frac{1}{2}(AIC_{minimum}-AIC_i)} = 0.93$, which serves as a proportional representation of the probability of the $i_{th}$ model minimizing information loss. Although the increase in $R^2$ values was not deemed significant, and the information criteria is somewhat inconclusive for discriminating between the four and five-term model, the five-term model was not viable, as it was not thermodynamically admissible, due to the negative leading coefficient of its highest power term. Therefore, the four-term model,

$$\psi = \sum_i \beta_6(\lambda_i-1)^6 + \beta_4(\lambda_i-1)^4 + \beta_3(\lambda_i-1)^3 + \beta_2(\lambda_i-1)^2 \text{ with } i = 1,2,3 \qquad (5)$$

was deemed appropriate for further study of the brain tissue dataset (see Table 1).

**Table 1**
Coefficients and accuracy of the strain energy density functions fitted using the cortex data. $R^2_T$, $R^2_C$, and $R^2_S$ are the $R^2$ values for tension, compression, and shear, respectively.

| Parameters | One-term | Two-term | Three-term | Four-term | Five-term |
|---|---|---|---|---|---|
| $\beta_2$ | 1.388 | 1.577 | 1.504 | 1.370 | 1.371 |
| $\beta_3$ | – | −8.760 | −12.93 | −14.34 | −14.36 |
| $\beta_4$ | – | – | – | 43.33 | 47.67 |
| $\beta_5$ | – | – | – | – | – |
| $\beta_6$ | – | – | – | 3113 | – |
| $\beta_7$ | – | – | – | – | – |
| $\beta_8$ | – | – | 472,338 | – | 535,184 |
| $\beta_9$ | – | – | – | – | – |
| $\beta_{10}$ | – | – | – | – | −26,336,688 |
| $R^2_T, R^2_C, R^2_S$ | 0.884, 0.251, 0.658 | 0.706, 0.718, 0.634 | 0.968, 0.947, 0.986 | 0.995, 0.994, 0.992 | 0.996, 0.995, 0.992 |
| AIC | −172.16 | −208.88 | −323.34 | −407.23 | −407.09 |
| Strain energy function's polyconvexity | Yes | No | No | Yes | No |

### 3.2. Model performance calibration

A modest, four-parameter material model was established through the regression of tension, compression, and shear data from the brain cortex leading to the polynomial strain energy function given by Equation (5). The proposed material model is now adjusted to the well-known benchmark data for the elastic response of human brain tissue (Budday et al., 2017a, 2017b, 2020; Linka et al., 2022; Pierre et al., 2023), fitting simultaneously to tension, compression, and shear data obtained from various regions of the brain, including the cortex, basal ganglia, corona radiata, and corpus callosum. The results are displayed in Fig. 2, with the model coefficients and regression accuracy for each brain region, measured by $R^2$, summarized in Table 2.

The combined illustration of Fig. 2 and Table 2 make clear that the four-parameter model expressed by Equation (5) is capable of accurately modeling the four brain tissues under examination, as evidenced by the $R^2$ values (no less than 0.984 for tension, 0.905 for compression, and 0.973 for shear) (see Table 2). Additionally, these results demonstrate that Equation (5) is well-equipped to handle the modeling of brain tissue undergoing multiple modes of deformation.

It is evident that the model under consideration, although displaying a certain degree of accuracy, is not flaw-free and the deviations it incurs are systematic in nature instead of random. The residuals from the regressions presented in Fig. 2 are depicted in Fig. 3. The systematic deviations show that the model is likely an underfitting of real brain tissue deformation data. For a well-fit model (neither under- nor overfitting) the residuals ($y_{data} - y_{model}$) are expected to be randomly distributed around zero and show no trend with the independent variable. As it manifests, the model tends to undervalue or overvalue stresses from individual deformations over large ranges of strain creating a trend in

**Table 2**
Parameters for Equation (5) used in Fig. 2 to describe stress-strain behavior of four brain regions. $R^2_T$, $R^2_C$, and $R^2_S$ are the $R^2$ values tension, compression, and shear respectively.

| Region | $\beta_2$ | $\beta_3$ | $\beta_4$ | $\beta_6$ | $R^2_T, R^2_C, R^2_S$ |
|---|---|---|---|---|---|
| Cortex | 1.370 | −14.34 | 43.33 | 3113 | 0.995, 0.994, 0.992 |
| Basal ganglia | 0.693 | −6.877 | 23.13 | 745.7 | 0.991, 0.983, 0.982 |
| Corona radiata | 0.731 | −9.544 | 26.43 | 1268 | 0.984, 0.942, 0.977 |
| Corpus callosum | 0.374 | −5.165 | 24.48 | 0 | 0.986, 0.905, 0.973 |

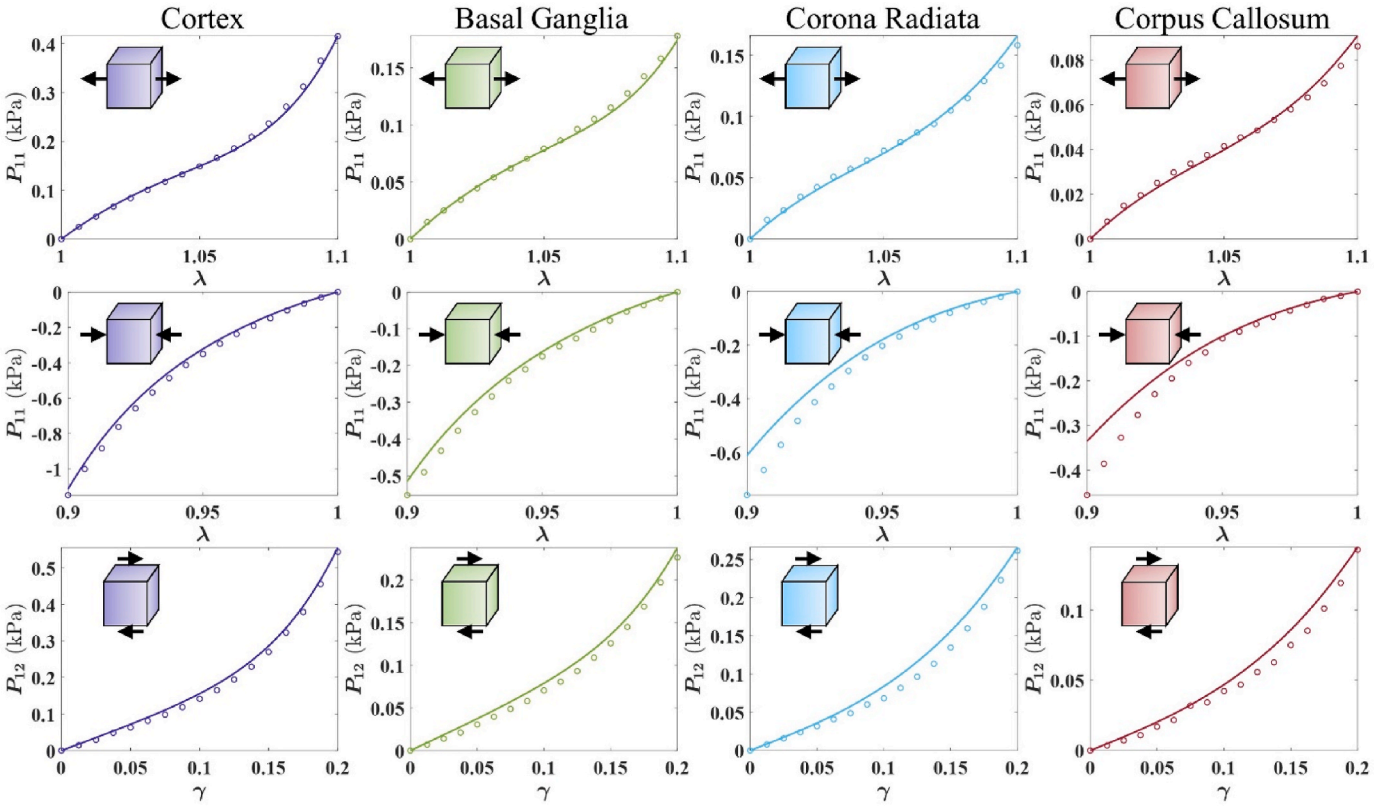


**Fig. 2.** Results from fitting Equation (5) (solid lines) against stress-strain data of brain tissue (scattered data). Each column of subfigures represent data from different regions of the brain: cortex (purple), basal ganglia (green), corona radiata (blue), and corpus callosum (red). Each row represents data from different deformation modes: tension (first row), compression (second row), shear (third row). For each brain region, Equation (5) is fitted using compression, tension, and shear data simultaneously.

the residuals. From the nature of underfitting, when calibrating this model, it is important to include different modes of deformation in the training process. Otherwise, the model will adjust to more accurately describe the deformation mode used for fitting at the expense of its ability to describe other deformation modes as evidenced in Fig. 4. In Fig. 4, because the model is underfitting, the deformation data used for fitting is well described with the model achieving $R^2$-values greater than 0.999 but the accuracy of the model drops when describing other deformation modes (see the description of compression when only shear data is regressed).

### 3.3. Accuracy and simplicity

The assessment of the proposed model continues with a comparison to competing models, as depicted in Fig. 5 These include the incompressible, isotropic four-parameter Ogden model, represented by $\psi^{Ogd} = \frac{\mu_1}{\alpha_1^*}(\lambda_1^{\alpha_1} + \lambda_2^{\alpha_1} + \lambda_3^{\alpha_1} - 3) + \frac{\mu_2}{\alpha_2^*}(\lambda_1^{\alpha_2} + \lambda_2^{\alpha_2} + \lambda_3^{\alpha_2} - 3)$, the two-parameter Gent model represented by $\psi^{Gnt} = -\frac{1}{2}\mu J_m \ln\left[1 - \frac{(\lambda_1^2+\lambda_2^2+\lambda_3^2-3)}{J_m}\right]$, and the two-parameter Demiray model represented by $\psi^{Dmr} = \frac{1}{2}\mu(\exp[\beta(\lambda_1^2 + \lambda_2^2 + \lambda_3^2 - 3)] - 1)/\beta$. We note that a successive combination of either multiple Gent or Demiray terms proves to be inconsequential as neither model effectively scales the stretches. Therefore, a like-to-like comparison with respect to the number of tunable model parameters cannot be conducted for these models in contrast to the Ogden model.

The four-parameter Ogden model proves to be superior in all deformation modes compared to the two-parameter Gent and Demiray models. Although both the proposed strain-energy function and the four-parameter Ogden model possess an equal number of adjustable parameters, the proposed model (Equation (5)) demonstrates greater accuracy in each individual deformation mode, as evidenced by $R^2$ values in Table 3. The average $R^2$ value for the four-parameter Ogden model is 0.9907 which is marginally less accurate than Equation (5) with an average $R^2$ value of 0.9937. However, the AIC of the four-parameter Ogden model is −382.69 vs the AIC of Equation (5) which is −407.23 giving a relative likelihood for the four-parameter Ogden model of $e^{\frac{1}{2}(-407.23+382.69)} = 4.69\times10^{-6}$ which serves as a proportional representation of the probability of the four-parameter Ogden model minimizes information loss. The Demiray and Gent models perform excellently in

**Table 3**
Results for regression of modified Ogden model, Gent model, and Demiray. As in Tables 1 and 2, $R_T^2$, $R_C^2$, and $R_S^2$ are the $R^2$ values tension, compression, and shear respectively.

| Equation (5), $\psi$ | | | | |
|---|---|---|---|---|
| $\beta_2$ | $\beta_3$ | $\beta_4$ | $\beta_6$ | $R_T^2, R_C^2, R_S^2$ |
| 1.370 | −14.34 | 43.33 | 3113 | 0.995, 0.994, 0.992 |
| Modified Ogden, $\psi^{Ogd}$ | | | | |
| $\mu_1$ | $\mu_2$ | $\alpha_1$ | $\alpha_2$ | $R_T^2, R_C^2, R_S^2$ |
| −0.128 | $4.8\times10^{-6}$ | −20.41 | 106.4 | 0.992, 0.991, 0.989 |
| Machine Learning, $\psi^{ML\lambda}$ | | | | |
| – | – | – | – | $R_T^2, R_C^2, R_S^2$ |
| – | – | – | – | 0.937, 0.985, 0.987 |
| Gent, $\psi^{Gnt}$ | | | | |
| $\mu$ | $J_m$ | – | – | $R_T^2, R_C^2, R_S^2$ |
| 1.200 | 0.0761 | – | – | 0.739, 0.572, 0.989 |
| Demiray, $\psi^{Dmr}$ | | | | |
| $\mu$ | $\beta$ | – | – | $R_T^2, R_C^2, R_S^2$ |
| 1.187 | 15.58 | – | – | 0.743, 0.552, 0.959 |
| Machine Learning, $\psi^{MLI_k}$ | | | | |
| – | – | – | – | $R_T^2, R_C^2, R_S^2$ |
| – | – | – | – | 0.356, 0.897, 0.985 |

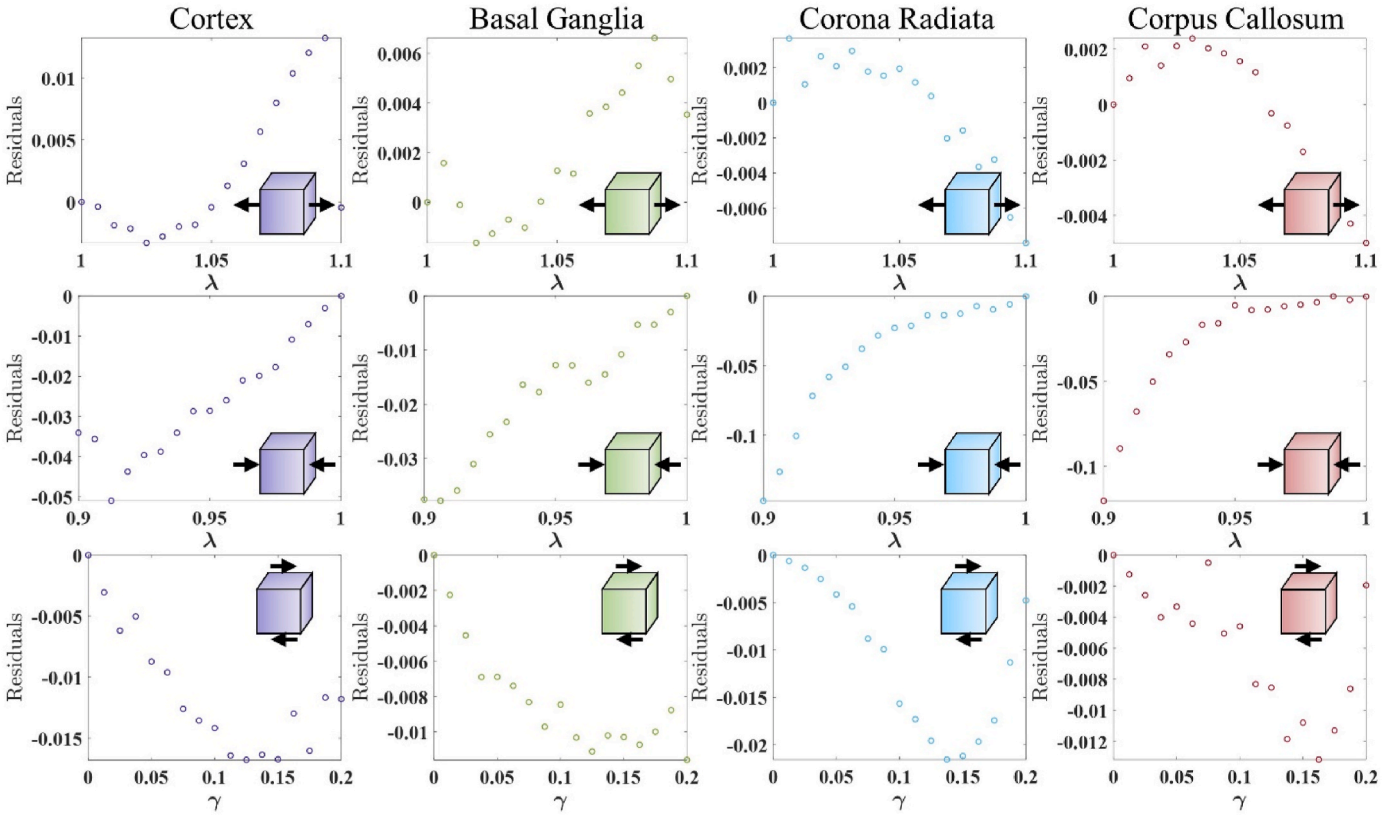


**Fig. 3.** Residual plots from the regressions in Fig. 2. The residuals are systematic instead of random showing the model is likely underfitting the brain tissue deformation data.

shear but fall short in capturing the nonlinearity of tensile and compressive deformations.

Recently, Linka et al. have developed a thermodynamics-based artificial network for constitutive equation discovery, which enforces, a priori, isotropy, incompressibility, the second law of thermodynamics, material objectivity, and strain energy polyconvexity (Linka and Kuhl, 2023). They have subsequently used the methodology to find constitutive equations for brain tissue elasticity (Linka et al., 2022; Pierre et al., 2023). The first of two neural networks considered strain energy densities as power functions of invariants $(I_1-3)^k$, $(I_2-3)^k$, strain energy densities as exponential functions of invariants $e^{\varphi_1(I_1-3)^k}-1$ and $e^{\varphi_2(I_2-3)^k}$, and the logarithmic functions invariants $-\ln(1-(I_1-3)^k)$ and $-\ln(1-(I_2-3)^k)$ ($\psi^{MLI_k}$ in Fig. 5 and Table 3). For the brain cortex, this machine learning model found a four-parameter equation achieving $R^2$ values of 0.897, 0.356, and 0.985 for compression, tension, and shear respectively. The results for basal ganglia, corona radiata, and corpus callosum were of lower quality, yielding less favorable $R^2$ values.

Their second neural network considered strain energy functions as a product of Ogden terms $\sum_{k=1}^{n}\frac{\mu_k}{\alpha_k}(\lambda_1^{\alpha_k}+\lambda_2^{\alpha_k}+\lambda_3^{\alpha_k}-3)$ ($\psi^{ML\lambda}$ in Fig. 5 and Table 3). The stretch-based machine learning models provided much higher accuracy fits at the cost of including more terms. The machine learning algorithm identified a 20-parameter, 16-parameter, 14-parameter, and 14-parameter model for the cortex, basal ganglia, corona radiata, and corpus callosum, respectively. The machine learned, multiparameter Ogden models perform with a similar accuracy as the model proposed here (within hundredths of the $R^2$ values achieved by Equation (5)). However, the large number of Ogden terms are needed to achieve this accuracy may have resulted to constraints placed on the neural network. In conclusion, the machine learning model performed with great accuracy, but the cost of this accuracy was an increased number of terms, and a different model for each region of the brain. The model proposed here describes each region of the brain accurately and outperforms the multiple term Ogden models found by the artificial neural network. A comparison of these results is included in Fig. 3 and Table 3; the strain energy density found by the network searching for power, exponential, and logarithmic functions is denoted $\psi^{MLI_k}$ and the strain energy density found by the Ogden network is denoted $\psi^{ML\lambda}$. We would also like to note that the stretch-based formulations of strain energy density (Equation (5), four-parameter Ogden, and Ogden network) as a group outperformed the invariant based formulations of strain energy density (Gent, Demiray, and invariant network).

In continuation of the discussion, it is clear that the future of material modeling will be dominated in part by machine learning methods, particularly for the swift identification of phenomenological constitutive equations possessing remarkable accuracy. Our proposed model, as demonstrated in Equation (5), may serve as a high-quality constitutive model for brain tissue elasticity in the short term and Equation (1) may serve as a contribution to machine learning toolkits in the future.

We note that we assumed homogeneous deformation states during testing in this work. As the specimens were glued to the specimen holders during the actual experiments, this may lead to a certain deviation in the material parameters due to inhomogeneous deformation (Budday et al., 2020). Therefore, in the future, an inverse parameter identification based on finite element simulations could be performed to identify even more accurate parameters for the new strain energy density function proposed here.

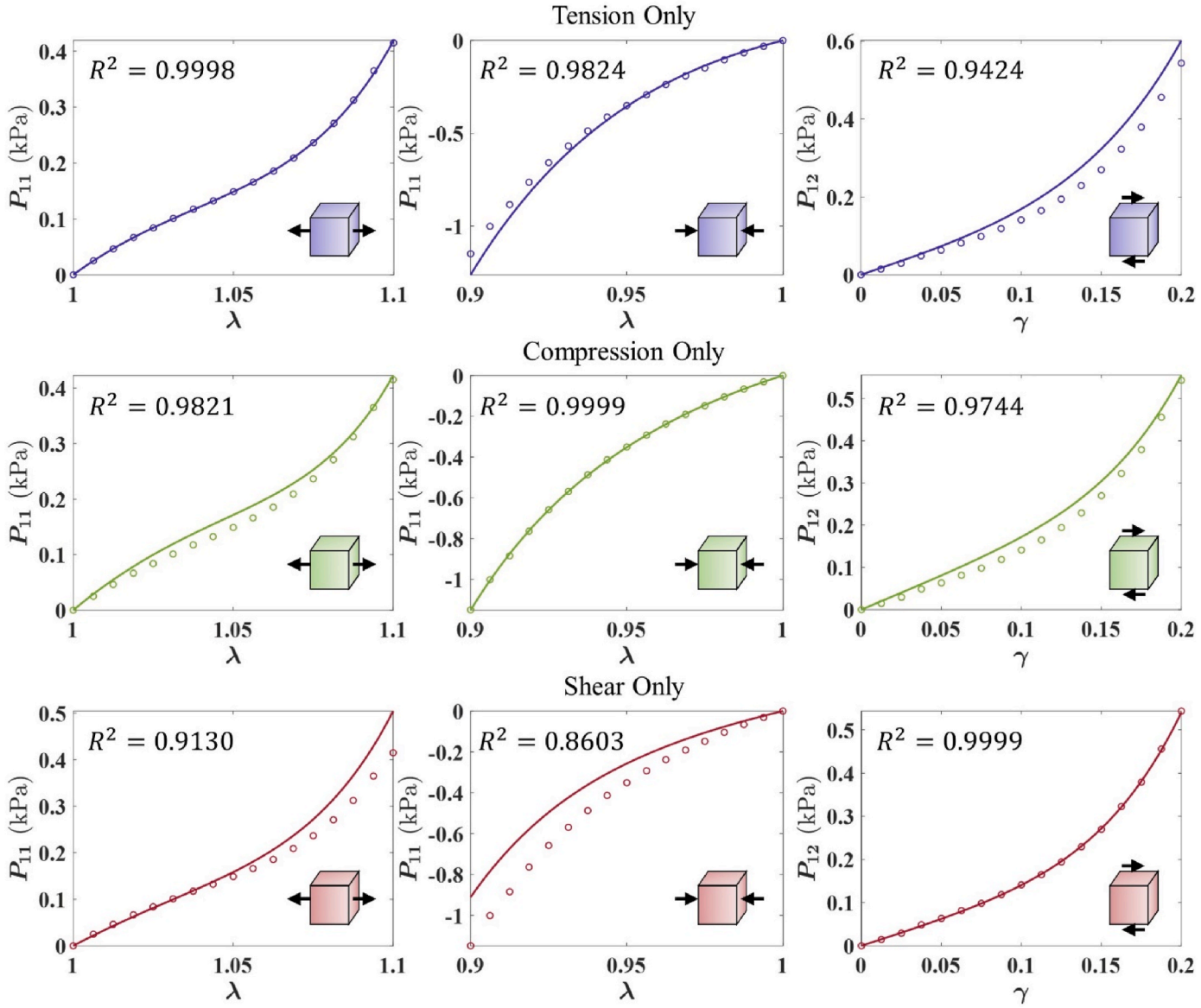


**Fig. 4.** Results from fitting Equation (5) (solid lines) against stress-strain data of the cortex (scattered data). These regressions were performed using a single dataset (tension, compression, or shear) to identify the model parameters. The first row is tension, compression, and shear data/fit using only tensile data for regression. The second row is tension, compression, and shear data/fit using only compression data for regression. The third row is tension, compression, and shear data/fit using only shear data for regression. The $R^2$-value for each model in each deformation mode is shown in the top-left corner of the corresponding plot.

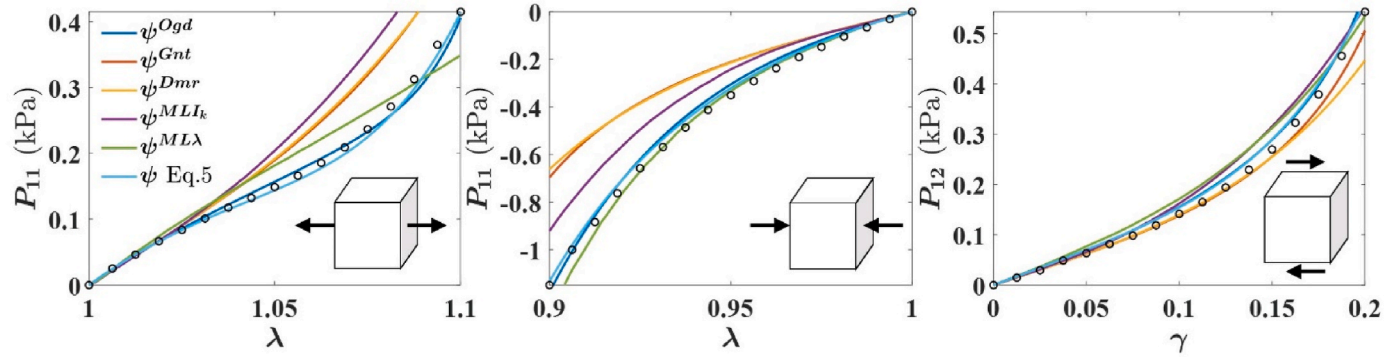


**Fig. 5.** The cortex data for compression, tension, and shear (black circles) were used to regress a four-parameter Ogden model, Gent model, and Demiray model. The results from two machine learning models ($MLI_k$ and $ML\lambda$) have been graphed as well alongside the model presented here.

## 4. Conclusions

In this paper, a general, hyperelastic, stretch-based potential was introduced, from which a specific four-parameter model was derived showing remarkable accuracy in modeling the mechanics of brain tissue. This model was calibrated to capture the time-independent behavior of four regions in the brain, namely the cortex, basal ganglia, corona radiata, and corpus callosum, encompassing their properties in compression, tension, and shear with a single model. Upon comparison to alternative models, such as the Ogden model, the Gent model, the Demiray model, as well as invariant and stretch-based machine learned models, it was found that this four-parameter model demonstrated a higher degree of accuracy in capturing brain tissue elasticity. This work holds potential in advancing our understanding of brain tissue elasticity and may prove to be a valuable asset in the investigation of brain morphologies, malformations, and injuries. The inclusion of this potential in the realm of automated material model discovery may lead to more precise predictions from machine learned models in the future.

## Competing financial interest

The authors declare no competing financial interests.

## CRediT authorship contribution statement

**Nicholas Filla:** Writing – review & editing, Writing – original draft, Methodology, Investigation, Formal analysis, Data curation. **Jixin Hou:** Writing – review & editing, Validation, Methodology, Data curation. **Tianming Liu:** Writing – review & editing, Funding acquisition. **Silvia Budday:** Writing – review & editing, Validation, Methodology, Funding acquisition. **Xianqiao Wang:** Writing – review & editing, Supervision, Funding acquisition, Conceptualization.

## Data availability

Data will be made available on request.

## Acknowledgement

This work is partially supported by National Science Foundation (IIS-2011369) and National Institutes of Health (1R01NS135574), as well as by the German Research Foundation (Deutsche Forschungsgemeinschaft, DFG) through the grant BU 3728/1-1.

## Appendix A

Kinematics - During deformation, a point with an original position $\boldsymbol{X}$ in the undeformed reference configuration moves to a new position $\boldsymbol{x}$ in the deformed configuration, a progression that may be represented by the deformation gradient, $\boldsymbol{F} = \frac{\partial \boldsymbol{u}}{\partial \boldsymbol{X}} + \boldsymbol{I}$, where the displacement vector $\boldsymbol{u}$ is equal to $\boldsymbol{x} - \boldsymbol{X}$ and $\boldsymbol{I}$ is the identity tensor. In evaluating the relationship between deformation and energy change, it is often beneficial to employ the right Cauchy-Green strain tensor $\boldsymbol{C} = \boldsymbol{F}^T\boldsymbol{F}$ and the left Cauchy-Green strain tensor $\boldsymbol{b} = \boldsymbol{F}\boldsymbol{F}^T$, as they eliminate the translational and rotational components present in the deformation gradient. Additionally, it is advantageous to consider the principal stretches, $\lambda_i$, which can be obtained from the left Cauchy-Green strain, $\boldsymbol{b} = \sum_{a=1}^{3}\lambda_a^2\boldsymbol{n}_a \otimes \boldsymbol{n}_a$, or from the right Cauchy-Green strain, $\boldsymbol{C} = \sum_{a=1}^{3}\lambda_a^2\boldsymbol{N}_a \otimes \boldsymbol{N}_a$, where $\otimes$ represents the tensor product. These tensors possess the same eigenvalues, $\lambda_a^2$, but different eigenvectors, the normalized principal directions $\boldsymbol{N}_a$ and $\boldsymbol{n}_a$ in undeformed and deformed configurations, respectively.

## Appendix B

Stress - The stresses in a hyperelastic material are found by considering the change in energy density due to deformation. Strain energy density, $\psi$, is a scalar quantity defined at every point in a material and its derivative with respect to various strain measures yields various stress measures. For an incompressible hyperelastic material model, the principal 1st Piola Kirchhoff stresses (engineering stresses) can be written as, $P_i = \frac{\partial \psi}{\partial \lambda_i} - \frac{p}{\lambda_i}$ with $i = 1,2,3$, where $p$ is an unknown hydrostatic pressure that represents a workless reaction to the incompressibility constraint place on the deformation field. The scalar $p$ is determined from the boundary conditions of a specific deformation mode. This definition of the 1st Piola Kirchhoff stress is convenient for the case of simple tension or compression. The 1st Piola Kirchhoff stress may also be written as a spectral decomposition, $\boldsymbol{P} = \sum_{a=1}^{3}P_a\widehat{\boldsymbol{n}}_a\bigotimes\widehat{\boldsymbol{N}}_a - \left(\sum_{a=1}^{3}p\lambda_a\widehat{\boldsymbol{n}}_a\bigotimes\widehat{\boldsymbol{N}}_a\right)^{-T}$ where $P_a = \frac{\partial \psi}{\partial \lambda_a}$, $\lambda_a$ are the principal stretches, $\widehat{\boldsymbol{n}}_a$ are the normalized eigenvectors of $\boldsymbol{b}$, and $\widehat{\boldsymbol{N}}_a$ are the normalized eigenvectors of $\boldsymbol{C}$. This definition of 1st Piola Kirchhoff stress is convenient for deriving shear stress.

In the occurrence of *uniaxial tension or compression*, the deformation gradient may be written as, $\boldsymbol{F} = diag[\lambda_1, \lambda_2, \lambda_3]$ where $\lambda_1$,$\lambda_2$,$\lambda_3$ are the principal stretches (square root of the eigenvalues of $\boldsymbol{b}$ or $\boldsymbol{C}$) and the eigenvectors of $\boldsymbol{b}$ or $\boldsymbol{C}$ happen to coincide with the experimental reference frame. The hydrostatic pressure due to the incompressibility assumption, $p$, can be deduced from either of the zero stress boundary conditions $P_2 = P_3 = 0$. Solving for $0 = P_2 = \frac{\partial \psi}{\partial \lambda_2} - \frac{p}{\lambda_2}$ gives $p = \lambda_2\frac{\partial \psi}{\partial \lambda_2}$. From the incompressibility condition $\det[\boldsymbol{F}] = 1 = \lambda_1\lambda_2\lambda_3$ and isotropy $\lambda_2 = \lambda_3$ we see that $\lambda_2 = \lambda_3 = 1/\sqrt{\lambda_1}$. Therefore, the first principal stress, which is equivalent to the normal stress in the direction of loading, is $P_1 = P_{11} = \frac{\partial \psi}{\partial \lambda_1} - \frac{1}{\lambda_1\sqrt{\lambda_1}}\frac{\partial \psi}{\partial \lambda_2}$. Finally, inserting the expressions for $\frac{\partial \psi}{\partial \lambda_1}$ and $\frac{\partial \psi}{\partial \lambda_2}$ yields Equation (2) in the main text.

For simple shear the deformation gradient is expressed in matrix representation as, $\boldsymbol{F} = \begin{bmatrix} 1 & \gamma & 0 \\ 0 & 1 & 0 \\ 0 & 0 & 1 \end{bmatrix}$. The left Cauchy Green tensor for simple shear is, $\boldsymbol{b} = \boldsymbol{F}\boldsymbol{F}^T = \begin{bmatrix} \gamma^2+1 & \gamma & 0 \\ \gamma & 1 & 0 \\ 0 & 0 & 1 \end{bmatrix}$ and has the following normalized eigenvectors,

$$\widehat{n}_1 = \begin{bmatrix} \dfrac{\gamma+\sqrt{4+\gamma^2}}{2\sqrt{1+\frac{1}{4}\left(\gamma+\sqrt{4+\gamma^2}\right)^2}} \\ \dfrac{1}{\sqrt{1+\frac{1}{4}\left(\gamma+\sqrt{4+\gamma^2}\right)^2}} \\ 0 \end{bmatrix}, \widehat{n}_2 = \begin{bmatrix} \dfrac{\gamma-\sqrt{4+\gamma^2}}{2\sqrt{1+\frac{1}{4}\left(\gamma-\sqrt{4+\gamma^2}\right)^2}} \\ \dfrac{1}{\sqrt{1+\frac{1}{4}\left(\gamma-\sqrt{4+\gamma^2}\right)^2}} \\ 0 \end{bmatrix}, \widehat{n}_3 = \begin{bmatrix} 0 \\ 0 \\ 1 \end{bmatrix} \tag{B1}$$

The right Cauchy Green tensor for simple shear is, $\boldsymbol{C} = \boldsymbol{F}^T\boldsymbol{F} = \begin{bmatrix} 1 & \gamma & 0 \\ \gamma & \gamma^2+1 & 0 \\ 0 & 0 & 1 \end{bmatrix}$ and has the following normalized eigenvectors,

$$\widehat{N}_1 = \begin{bmatrix} \dfrac{-\gamma+\sqrt{4+\gamma^2}}{2\sqrt{1+\frac{1}{4}\left(-\gamma+\sqrt{4+\gamma^2}\right)^2}} \\ \dfrac{1}{\sqrt{1+\frac{1}{4}\left(-\gamma+\sqrt{4+\gamma^2}\right)^2}} \\ 0 \end{bmatrix}, \widehat{N}_2 = \begin{bmatrix} \dfrac{-\gamma-\sqrt{4+\gamma^2}}{2\sqrt{1+\frac{1}{4}\left(-\gamma-\sqrt{4+\gamma^2}\right)^2}} \\ \dfrac{1}{\sqrt{1+\frac{1}{4}\left(-\gamma-\sqrt{4+\gamma^2}\right)^2}} \\ 0 \end{bmatrix}, \widehat{N}_3 = \begin{bmatrix} 0 \\ 0 \\ 1 \end{bmatrix} \tag{B2}$$

By definition $P_a = \frac{\partial\psi}{\partial\lambda_a}$ so the shear stress, $P_{12}$, is given by,

$$P_{12} = \left(\frac{\gamma+\sqrt{4+\gamma^2}}{2\sqrt{1+\frac{1}{4}\left(\gamma+\sqrt{4+\gamma^2}\right)^2}}\right)\left(\frac{1}{\sqrt{1+\frac{1}{4}\left(-\gamma+\sqrt{4+\gamma^2}\right)^2}}\right)\frac{\partial\psi}{\partial\lambda_1} + \left(\frac{\gamma-\sqrt{4+\gamma^2}}{2\sqrt{1+\frac{1}{4}\left(\gamma-\sqrt{4+\gamma^2}\right)^2}}\right)\left(\frac{1}{\sqrt{1+\frac{1}{4}\left(-\gamma-\sqrt{4+\gamma^2}\right)^2}}\right)\frac{\partial\psi}{\partial\lambda_2} - \left(\sum_{a=1}^{3} p\lambda_a\widehat{\boldsymbol{n}}_a\otimes\widehat{\boldsymbol{N}}_a\right)^{-T} \tag{B3}$$

The 12-component of the penalty function $\sum_{a=1}^{3} p(\lambda_a\widehat{\boldsymbol{n}}_a\otimes\widehat{\boldsymbol{N}}_a)^{-T}$ evaluates to zero. The principal stretches are the square root of the eigenvalues of either $\boldsymbol{C}$ or $\boldsymbol{b}$ and were found to be $\lambda_1 = \sqrt{\frac{1}{2}(2+\gamma^2+\gamma\sqrt{4+\gamma^2})}$, $\lambda_2 = \frac{1}{\lambda_1} = \sqrt{\frac{1}{2}(2+\gamma^2-\gamma\sqrt{4+\gamma^2})}$, and $\lambda_3 = 1$. Upon careful examination and substitution, the equation for shear stress simplifies to $P_{12} = \frac{\lambda_1^2}{\lambda_1^2+1}\frac{\partial\psi}{\partial\lambda_1} - \frac{\lambda_2^2}{\lambda_2^2+1}\frac{\partial\psi}{\partial\lambda_2}$. Finally, inserting the expressions for $\frac{\partial\psi}{\partial\lambda_1}$ and $\frac{\partial\psi}{\partial\lambda_2}$ and substituting $\frac{1}{\lambda_1}$ for all instances of $\lambda_2$ yields Equation (3) in the main text.

## Appendix C

Consistency with Linear Elasticity - In isotropic linear elasticity the relationship between stress $\sigma$ and strain $\varepsilon$ is, $\sigma_{ij} = \lambda\varepsilon_{kk}\delta_{ij} + 2\mu\varepsilon_{ij}$, where $\lambda$ and $\mu$ are Lame's constants and $\delta_{ij}$ is Kronecker's delta. For shear stress at small strains we can write, $\sigma = 2\mu\gamma$, and this gives the condition that, $\frac{\partial\sigma}{\partial\gamma} = 2\mu$. Replacing $\sigma$ with the nonlinear, hyperelastic shear stress and taking the limit of $\frac{\partial\sigma}{\partial\gamma} = 2\mu$ as $\gamma$ approaches zero provides a condition for the hyperelastic potential to be consistent with linear elasticity. Note: at small strains, especially at zero strain, the distinction between stress measures vanishes so we can replace $\sigma$ with the first Piola-Kirchoff shear stress given in equation (3) of the main text. Therefore,

$$\lim_{\gamma\to 0}\left[\frac{\partial}{\partial\gamma}\left(k\beta_k\left(\frac{\lambda^2}{\lambda^2+1}(\lambda-1)^{k-1} - \frac{\lambda^{-2}}{\lambda^{-2}+1}\left(\frac{1}{\lambda}-1\right)^{k-1}\right)\right)\right] = 2\mu \tag{C1}$$

and this limit evaluates to, $\frac{k}{2}\beta_k(0^{k-2}(k-1) + 0^{k-1}) = 2\mu$. The indeterminate form $0^0$ is a controversial topic, and there's no universally accepted value for it. However, in some contexts, it's convenient to define $0^0 = 1$. It is left to the reader to accept or decline this definition. From this it follows if $k = 1$ then the expression evaluates to $\frac{1}{2}\beta_k\left(\frac{0}{0}+0^0\right)$ and is therefore undefined. If $k = 2$ then the expression evaluates to $\beta_k(0^0 + 0^1) = \beta_k$. If $k > 2$ then the expression is zero. Therefore, the shear modulus of this model is $\frac{\beta_2}{2}$ and the model should no include the term for $k = 1$.

## References


Barnes, J.M., Przybyla, L., Weaver, V.M., 2017. Tissue mechanics regulate brain development, homeostasis and disease. J. Cell Sci. 130 (1), 71–82.

Blümcke, I., Vinters, H.V., Armstrong, D., Aronica, E., Thom, M., Spreafico, R., 2009. Malformations of cortical development and epilepsies. Epileptic Disord. 11 (3), 181–193.

Blumenthal, N.R., Hermanson, O., Heimrich, B., Shastri, V.P., 2014. Stochastic nanoroughness modulates neuron–astrocyte interactions and function via mechanosensing cation channels. Proc. Natl. Acad. Sci. U.S.A. 111 (45), 16124–16129.

Budday, S., Raybaud, C., Kuhl, E., 2014. A mechanical model predicts morphological abnormalities in the developing human brain. Sci. Rep. 4 (1), 1–7.

Budday, S., Steinmann, P., Kuhl, E., 2015. Physical biology of human brain development. Front. Cell. Neurosci. 9, 257.

Budday, S., Sommer, G., Birkl, C., Langkammer, C., Haybaeck, J., Kohnert, J., Bauer, M., Paulsen, F., Steinmann, P., Kuhl, E., 2017a. Mechanical characterization of human brain tissue. Acta Biomater. 48, 319–340.

Budday, S., Sommer, G., Haybaeck, J., Steinmann, P., Holzapfel, G.A., Kuhl, E., 2017b. Rheological characterization of human brain tissue. Acta Biomater. 60, 315–329.
Budday, S., Ovaert, T.C., Holzapfel, G.A., Steinmann, P., Kuhl, E., 2020. Fifty shades of brain: a review on the mechanical testing and modeling of brain tissue. Arch. Comput. Methods Eng. 27, 1187–1230.
Destrade, M., Saccomandi, G., Sgura, I., 2017. Methodical fitting for mathematical models of rubber-like materials. Proc. R. Soc. A 473 (2198), 20160811.
Faul, M., Wald, M.M., Xu, L., Coronado, V.G., 2010. Traumatic Brain Injury in the United States: Emergency Department Visits, Hospitalizations, and Deaths, 2002-2006.
Goriely, A., Geers, M.G., Holzapfel, G.A., Jayamohan, J., Jérusalem, A., Sivaloganathan, S., Squier, W., van Dommelen, J.A., Waters, S., Kuhl, E., 2015. Mechanics of the brain: perspectives, challenges, and opportunities. Biomech. Model. Mechanobiol. 14, 931–965.
Harrison, P.J., 1999. The neuropathology of schizophrenia: a critical review of the data and their interpretation. Brain 122 (4), 593–624.
Jalil Razavi, M., Zhang, T., Liu, T., Wang, X., 2015. Cortical folding pattern and its consistency induced by biological growth. Sci. Rep. 5 (1), 14477.
Linka, K., Kuhl, E., 2023. A new family of Constitutive Artificial Neural Networks towards automated model discovery. Comput. Methods Appl. Mech. Eng. 403, 115731.
Linka, K., Pierre, S.R. St, Kuhl, E., 2022. Automated model discovery for human brain using constitutive artificial neural networks. bioRxiv. https://doi.org/10.1101/2022.11.08.515656v1, 2022.11. 08.515656.
MacManus, D.B., Murphy, J.G., Gilchrist, M.D., 2018. Mechanical characterisation of brain tissue up to 35% strain at 1, 10, and 100/s using a custom-built micro-indentation apparatus. J. Mech. Behav. Biomed. Mater. 87, 256–266.
Majdan, M., Plancikova, D., Brazinova, A., Rusnak, M., Nieboer, D., Feigin, V., Maas, A., 2016. Epidemiology of traumatic brain injuries in Europe: a cross-sectional analysis. Lancet Public Health 1 (2), e76–e83.
Mihai, L.A., Chin, L., Janmey, P.A., Goriely, A., 2015. A comparison of hyperelastic constitutive models applicable to brain and fat tissues. J. R. Soc. Interface 12 (110), 20150486.
Nordahl, C.W., Dierker, D., Mostafavi, I., Schumann, C.M., Rivera, S.M., Amaral, D.G., Van Essen, D.C., 2007. Cortical folding abnormalities in autism revealed by surface-based morphometry. J. Neurosci. 27 (43), 11725–11735.
Pierre, S.R. St, Linka, K., Kuhl, E., 2023. Principal-stretch-based constitutive neural networks autonomously discover a subclass of Ogden models for human brain tissue. bioRxiv, 2023.01. 14.524079.
Rashid, B., Destrade, M., Gilchrist, M.D., 2014. Mechanical characterization of brain tissue in tension at dynamic strain rates. J. Mech. Behav. Biomed. Mater. 33, 43–54.
Razavi, M.J., Zhang, T., Li, X., Liu, T., Wang, X., 2015. Role of mechanical factors in cortical folding development. Phys. Rev. 92 (3), 032701.
Tallinen, T., Chung, J.Y., Rousseau, F., Girard, N., Lefèvre, J., Mahadevan, L., 2016. On the growth and form of cortical convolutions. Nat. Phys. 12 (6), 588–593.